

Physics-guided curriculum learning for the identification of reaction–diffusion dynamics from partial observations

Hanyu Zhou¹, Yuansheng Cao² and Yaomin Zhao^{1*}

¹HEDPS, Center for Applied Physics and Technology, and School of Mechanics and Engineering Science, Peking University, Beijing, 100871, China.

²Department of Physics, Tsinghua University, Beijing, 100084, China.

*Corresponding author(s). E-mail(s): yaomin.zhao@pku.edu.cn;

Contributing authors: hanyuzhou@stu.pku.edu.cn; yscao@tsinghua.edu.cn;

Abstract

Reaction–diffusion (RD) systems provide fundamental models for understanding self-organized spatiotemporal patterns across diverse natural and engineered settings, but reliable parameter estimation remains challenging, particularly when observations are sparse, noisy, and restricted to a subset of state variables. Based on physics-informed neural networks (PINNs), a physics-guided Curriculum Learning Identification via PINNs (CLIP) method is introduced in this work, for joint parameter inference and hidden state reconstruction. Leveraging the physical separability of RD systems, the CLIP training progresses from reaction-dominated regimes to full spatiotemporal dynamics using curriculum learning and an anchored widening transfer strategy. Across three canonical reaction–diffusion benchmarks, CLIP achieves more accurate and robust identification than baseline methods. Furthermore, the CLIP framework is successfully applied to infer the dynamics of Min system in bacteria, where only membrane bound species are observed and key kinetic rates span multiple orders of magnitude. Moreover, ablation experiments and loss landscape analyses provide mechanistic evidence that the curriculum stages and anchored transfer enhance trainability and convergence.

Keywords: parameter identification, partial observations, curriculum learning, transfer learning

1 Introduction

Many dynamical systems in physics, engineering, and biology are only partially observable in experiments [1–3]. Measurements often cover only a subset of state variables, while the unobserved components still interact nonlinearly with the measured ones. Under such partial state access, identifying governing parameters becomes intrinsically fragile, because multiple latent state trajectories can explain the same observations, making inference effectively ill-posed even when the model

structure is largely known. A representative example is oscillation in bacteria Min system [2], where membrane associated species are readily fluorescently labeled, yet cytosolic pools remain difficult to quantify. These challenges have motivated a growing body of work on parameter identification and state reconstruction under partial state observations.

Recent advances in machine learning have facilitated the identification of dynamical systems

from partial state observations. One direction primarily formulates the task as a forecasting problem and leverages deep learning models to predict state evolution [4, 5]. While such approaches often demonstrate strong predictive performance, they tend to compromise interpretability and require substantial pretraining. An alternative direction aims to explicitly recover the underlying governing dynamics by incorporating physical knowledge. Prevailing strategies generally rely on either sparse selection of predefined libraries [6, 7] or delay-coordinate embeddings motivated by Takens' theorem [8–10]. Despite the impressive capabilities of dynamical system identification, these approaches are most effective for ordinary differential equations (ODEs) that admit a low-dimensional representation. For partial differential equations (PDEs), recent advances in physics-informed neural networks (PINNs) provide a more direct route to system identification. By enforcing PDE residuals as soft constraints, PINNs enable the recovery of unknown physical parameters even under partial state observations [11, 12]. Nevertheless, optimization remains a major bottleneck for PINNs [13–15]. With partial and noisy observations, the inverse problem becomes weakly constrained and ill-conditioned, which can reduce training stability and hinder reliable parameter identification.

Among PDE models, reaction–diffusion (RD) systems are widely used due to their success in explaining pattern formation across chemistry [16], biology [17–19], ecology [20], and materials science [21, 22]. Accurately identifying RD parameters remains challenging, particularly under partial observations. This difficulty arises partly because RD patterns are often governed by stiff and nonlinear dynamics, where steep gradients and fine-scale features render the system highly sensitive to parameter variations. As demonstrated in Fig. 1a, even small perturbations in parameters can induce large qualitative changes in spatiotemporal patterns under identical initial conditions. This sensitivity intensifies under partial and noisy observations, particularly when the patterns contain sharp fronts and fine-scale structures, leading to a rugged and non-convex optimization landscape. Consequently, obtaining robust parameter estimates for RD systems remains a significant and unresolved challenge.

To overcome these ill-posedness barriers, we introduce physics-guided Curriculum Learning Identification via PINNs (CLIP), a framework that couples curriculum learning [23, 24] with PINNs for the identification of partially observed RD systems. Exploiting the spatiotemporal separability of RD patterns, the core idea of CLIP is to decouple the identification of local reaction kinetics from global diffusion coefficients. This curriculum design decomposes learning into progressively more challenging subproblems that reflect the underlying physics, as shown in Fig. 1b, enabling a gradual recovery of the governing RD dynamics. Specifically, by treating the reaction-dominated regime as a physical prior, we initially relax spatial coupling, forcing the network to resolve the nonlinear reaction topology through an approximate local ODE system. Once the local reaction kinetics are established, we progressively reintroduce the diffusion operator to recover the full PDE dynamics. Crucially, to bridge the transition from the local ODE limit to the global PDE formulation, we employ an anchored widening transfer strategy, as shown in Fig. 1c. This strategy improves training stability throughout the transition, preventing the high-variance gradients induced by diffusion residuals from destabilizing the learned reaction features. We validate CLIP on benchmark RD systems and a realistic high-dimensional biological oscillator, demonstrating that the physics-guided operator decoupling yields robust reconstruction of latent variables and accurate parameter recovery, even under regimes of high noise and partial observability.

2 Results

In general, an RD system is described by semi-parabolic partial differential equations of the form

$$\frac{\partial \mathbf{u}}{\partial t} = \mathbf{D} \Delta \mathbf{u} + \mathcal{F}(\mathbf{u}; \boldsymbol{\kappa}), \quad (1)$$

where $\mathbf{u} : \Omega \times (0, T] \rightarrow \mathbb{R}^N$ denotes the vector of state variables, $\mathbf{x} \in \Omega \subset \mathbb{R}^d$ is the spatial coordinate, $t \in (0, T]$ is the time variable. Here $\Delta = \sum_{i=1}^d \partial^2 / \partial x_i^2$ denotes the Laplacian. $\mathbf{D} = \text{diag}(D_1, \dots, D_N)$ collects the diffusion coefficients, and $\boldsymbol{\kappa}$ denotes the unknown reaction parameters in \mathcal{F} . Under partial observability, only a subset of the state variables is accessible through

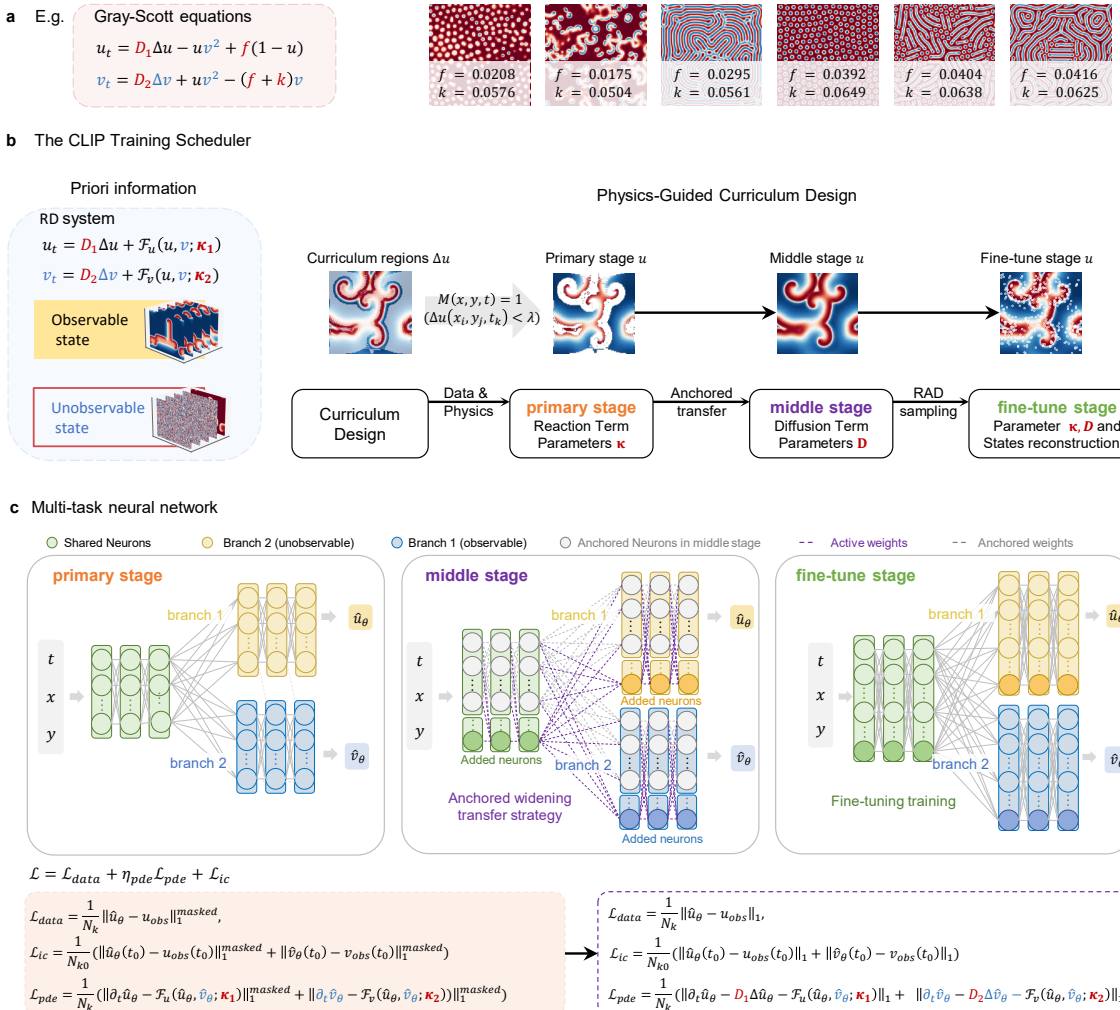


Fig. 1 The proposed CLIP framework. a, Representative spatiotemporal pattern types generated by the two-dimensional Gray-Scott reaction–diffusion model. **b**, Overview of the physics-induced Curriculum Learning Identification via PINNs (CLIP) training scheduler illustrated using a two-variable reaction–diffusion system. A physics-guided curriculum design stratifies the training data and associated physics constraints into a sequence of progressively more challenging subtasks. Curriculum regions are defined using Δu , the Laplacian of the observed field. The Gray–Scott system is shown as an example using a snapshot of the u field at time step $t_s = 600$. CLIP proceeds through three stages (primary, middle and fine-tuning stages), which successively identify reaction parameters, estimate diffusion coefficients, and jointly refine parameters and state reconstructions. **c**, Architecture and training strategy of the multi-task neural network. A shared spatiotemporal encoder takes coordinates (x, t) as input, followed by one task-specific branch for each state variable. Observable states are directly constrained by data losses, while unobserved states are reconstructed jointly through physics-based coupling. Training is conducted in multiple stages, during which different subsets of data and physics constraints are progressively activated. The losses \mathcal{L}_{data} , \mathcal{L}_{pde} , and \mathcal{L}_{ic} denote data mismatch, PDE residual, and initial-condition consistency, respectively. N_k denotes the number of spatiotemporal training points $\{(\mathbf{x}_k, t_k)\}_{k=1}^{N_k}$. The data losses in primary stage are evaluated on reaction-dominated samples selected by a spatiotemporal mask. Detailed definitions of the losses and mask construction are provided in Methods.

noisy measurements, while the remaining components are unobserved.

To address the inverse problem with limited observations, a curriculum learning strategy is

integrated into the PINN framework. The curriculum proceeds in three stages, progressively extending from reaction-dominated dynamics to the full RD system (See Methods 4.1). In the primary stage, reaction parameters are inferred from

regions where the local dynamics can be approximated by decoupled ODE behavior at each spatial location, using sufficiently long time series observations motivated by Takens' embedding theory [8]. Then diffusion parameters are introduced and optimized using an anchored widening transfer strategy to maintain training stability. Since diffusion-dominated dynamics are localized near narrow interfaces, uniform sampling can produce an imbalanced training set with few informative points. We therefore apply the residual-based adaptive distribution (RAD) sampling [25] to enhance the training dataset, and then fine-tune all parameters jointly.

Assuming that only a subset of the state variables is observed, we jointly infer the unobserved state trajectories and the unknown coefficients initialized randomly in $[0, 1]$. When initial conditions for the unobserved state variables are available, we include them as additional constraints, since partial observability can lead to non-unique solutions and unstable parameter estimates. We consider both clean data and data with 5% to 10% Gaussian noise. The CLIP framework is compared with a standard PINN, the ensemble Kalman filter (EnKF) [26], and particle swarm optimization (PSO) [27]. We also report relative absolute errors (RAE) for ablation studies that start from a baseline PINN, then introduce curriculum learning, and finally add the widthwise anchored transfer strategy. Further implementation details and experimental settings are given in the Methods and Supplementary Information.

2.1 Progressive discovery of hidden dynamics in chaotic and coupled systems

The λ - ω reaction-diffusion system

We first consider the λ - ω reaction-diffusion system as a canonical testbed to validate the feasibility of recovering hidden dynamics. This system exhibits smooth oscillatory behavior with relatively weak coupling between parameters, making it suitable as a proof-of-concept benchmark. From observations of a single variable u , CLIP accurately identifies the governing parameters and reconstructs the unobserved field v (Fig. 2a). Furthermore, simulations using the identified parameters closely reproduce the reference trajectories,

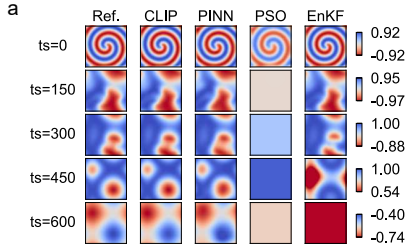
confirming physical consistency (Fig. 2b). Note that in this relatively simple setting, a standard PINN already provides strong performance, while PSO show limited convergence under partial observations. Although EnKF performs well with clean data, it is more sensitive to measurement noise as shown in Table 1. Incorporating curriculum learning and anchored widening transfer learning yields a modest but consistent improvement, establishing a reliable framework for more challenging systems (Fig. 2c).

The Gray-Scott equations

We next examine the Gray-Scott equations, which are characterized by strong nonlinearity, parameter sensitivity, and sharp reaction fronts associated with pattern formation. These features make optimization under partial observability particularly challenging. Under only measurements of u , CLIP achieves stable and accurate identification of all parameters across multiple noise levels as presented in Table 1. While the baseline PINN reproduces similar spatial structures, it exhibits noticeable quantitative errors, and both PSO and EnKF fail to converge without access to state v as shown in Fig. 2d. Furthermore, time-series comparisons in Fig. 2e demonstrate that CLIP captures the transient spike-like dynamics typical of this stiff regime. Moreover, an ablation study in Fig. 2f indicates that a direct transition to the high gradient regime destabilizes parameters that had previously converged. The instability arises because the emergence of sharp fronts changes both the data fitting objective and the balance among PDE residual terms. In this situation, the optimizer can reduce the loss more rapidly by adjusting reaction coefficients rather than updating network parameters, which leads to parameter compensation and drift. In contrast, the anchored transfer learning preserves parameter stability during the nonlinear transition, enabling consistent convergence in PDE setting.

The Lotka-Volterra equations

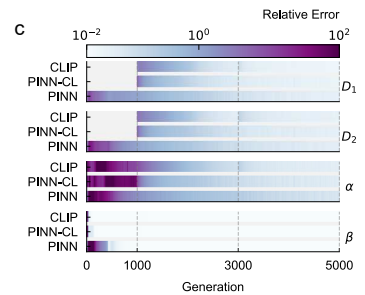
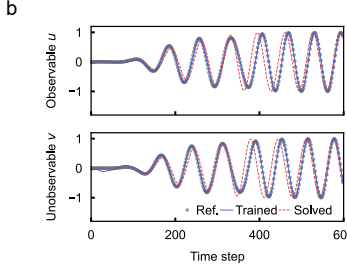
Finally, we consider the Lotka-Volterra reaction-diffusion equations, which involve six unknown parameters and strong coupling between reaction and diffusion processes. Across all tested noise levels, CLIP achieves consistently lower

$\lambda - \omega$ RD

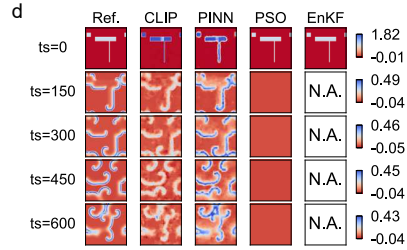
$$u_t = D_1 \Delta u + \alpha(1 - v^2 - u^2)u - \beta(v^2 + u^2)v$$

$$v_t = D_2 \Delta v + \alpha(1 - v^2 - u^2)v + \beta(v^2 + u^2)u$$

Ref : $D_1 = 1.00, D_2 = 1.00, \alpha = 1.00, \beta = -1.00$
 CLIP : $D_1 = 0.95, D_2 = 0.92, \alpha = 0.91, \beta = -1.00$

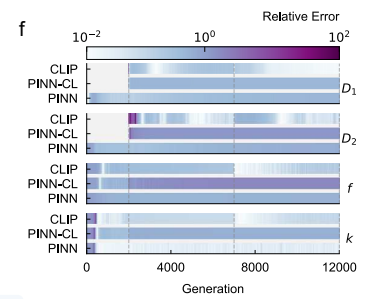
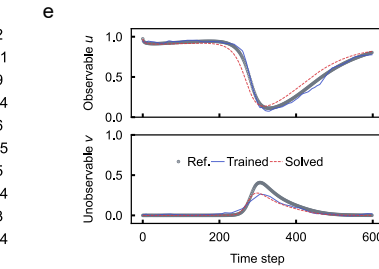


Gray-Scott

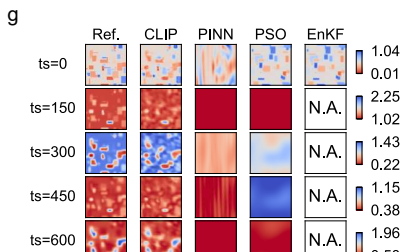


$$u_t = D_1 \Delta u - uv^2 + f(1 - u)$$

$$v_t = D_2 \Delta v + uv^2 - (f + k)v$$



Lotka-Volterra



$$u_t = D_1 \Delta u + \alpha u + \beta uv$$

$$v_t = D_2 \Delta v + \gamma uv + \epsilon v$$

Ref : $D_1 = 0.05, D_2 = 0.10, \alpha = 2.33, \beta = -2.67, \gamma = 1.00, \epsilon = -1.00$
 CLIP : $D_1 = 0.04, D_2 = 0.07, \alpha = 2.36, \beta = -2.70, \gamma = 0.98, \epsilon = -0.99$

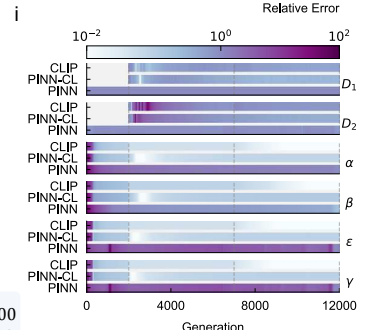
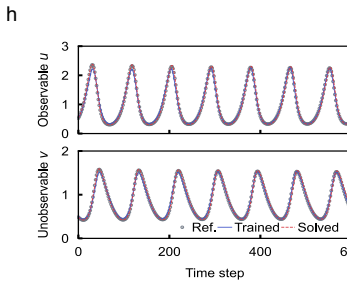


Fig. 2 Performance of CLIP framework on three reaction–diffusion systems. In the governing equations, variables shown in blue are unobserved, and parameters shown in red are inferred. a–c, Results on the $\lambda - \omega$ system; d–f, Gray–Scott; g–i, Lotka–Volterra. a,d,g, Reconstructed unobservable fields with comparisons to baseline methods. b,e,h, Single-point time series at the domain center. c,f,i, Relative errors of identified parameters from ablation on curriculum learning and anchored widening transfer learning.

identification errors in Table 1. Moreover, CLIP reconstructs time series that match both the amplitude and frequency of the reference solution shown in Fig. 2g,h. In contrast, PSO and EnKF do not reach an acceptable error level in our experiments. The baseline PINN exhibits large errors which are attributed to a compensation

mechanism between the reconstructed amplitude of the unobserved state v and the diffusion parameters. Since v is not observed beyond the initial condition, its amplitude is primarily determined by the PDE constraints during training. The amplitude of v in early optimization is usually underestimated, because the network tend to

Table 1 CLIP identification results: the relative absolute error of coefficients on canonical models

Noise	λ-ω RD			Gray-Scott			Lotka-Volterra		
	0	5%	10%	0	5%	10%	0	5%	10%
CLIP	5.50%	6.25%	11.5%	9.55%	21.77%	25.27%	9.23%	13.84%	16.09%
PINN	7.75%	9.50%	11.75%	120.33%	110.94%	70.58%	2703.09%	1685.24%	2169.26%
PSO	153.06%	146.77%	351.17%	2312.39%	-	-	1215.81%	1215.50%	1217.05%
ENKF	0.48%	-	-	-	-	-	-	-	-

fit low-frequency and low-amplitude components first. The loss may decrease more rapidly by increasing diffusion coefficients to reduce residuals, rather than by correcting the reconstructed signal, which biases the diffusion estimates. Ablation results in Fig. 2i further indicate that the primary stage provides a reliable initialization by focusing on reaction-dominated regions, and that the subsequent transfer stage improves stability and consistency of parameter identification.

2.2 Identification of high-dimensional biological systems

To evaluate CLIP on a realistic numerical experiment, we study protein self-organization in *Escherichia coli* that gives rise to oscillatory spatiotemporal patterns. In this system, MinD and MinE proteins undergo pole-to-pole oscillations to determine the cell division site. Based on established biochemical mechanisms, Loose et al. [2] proposed an RD model which reproduces key experimental observations by coupling cytosolic and membrane-bound protein dynamics. The model comprises four coupled reaction-diffusion equations for the cytosolic concentrations (c_D, c_E) and membrane-bound species (c_d, c_{de}). It includes five kinetic parameters and four diffusion coefficients as described in Fig. 3a. All kinetic rates and diffusion coefficients are treated as unknowns and inferred from data. In experiments, only the membrane-bound protein distributions (c_d, c_{de}) are accessible via fluorescence microscopy, while the cytosolic concentrations (c_D, c_E) are unobserved. To match this setting, training is performed using membrane data only, while jointly reconstructing the cytosolic states during training.

During the primary stage, optimization in log parameter space and residual scaling using a

characteristic concentration enable reliable identification of kinetic rates spanning several orders of magnitude as shown in Fig. 3a. On clean data, CLIP achieves a relative absolute error of 18.10%, whereas the baseline PINN reaches 72.15% and shows unstable optimization. With 10% additive Gaussian noise, CLIP maintains an RAE of 23.34%, indicating robustness in this high dimensional inverse problem. The reconstructed cytosolic protein distributions closely match the reference solution in Fig. 3b, and the time series at a representative spatial location reproduce both oscillation amplitudes and frequencies in Fig. 3c. An ablation study (Fig. 3d) highlights the importance of staged training. The large deviations observed in the baseline PINN reflect the intrinsic complexity of the Min oscillatory dynamics and the severe ill-conditioning of the inverse problem under partial observability.

To understand why CLIP remains trainable whereas the baseline PINN is prone to optimization failure, we further visualize the loss landscape and project training trajectories following Li et al. [28]. This technique captures variations in optimization trajectories within extremely low-dimensional subspaces. Artificial neural networks are usually optimized by minimizing a loss function over a large set of trainable parameters θ , thus giving rise to an inherently high-dimensional loss landscape. To give an intuitive visualization of the loss landscape and optimization paths, principal component analysis (PCA) is employed to project the high-dimensional trajectories onto a two-dimensional subspace. The procedure for generating these trajectories is described in Method 4.6. The projected trajectories on the first two principal components, together with contours of the loss surface, are shown in Fig. 4. For the baseline PINN (Fig. 4a), the projected loss surface contains multiple local basins, and the optimizer trajectory

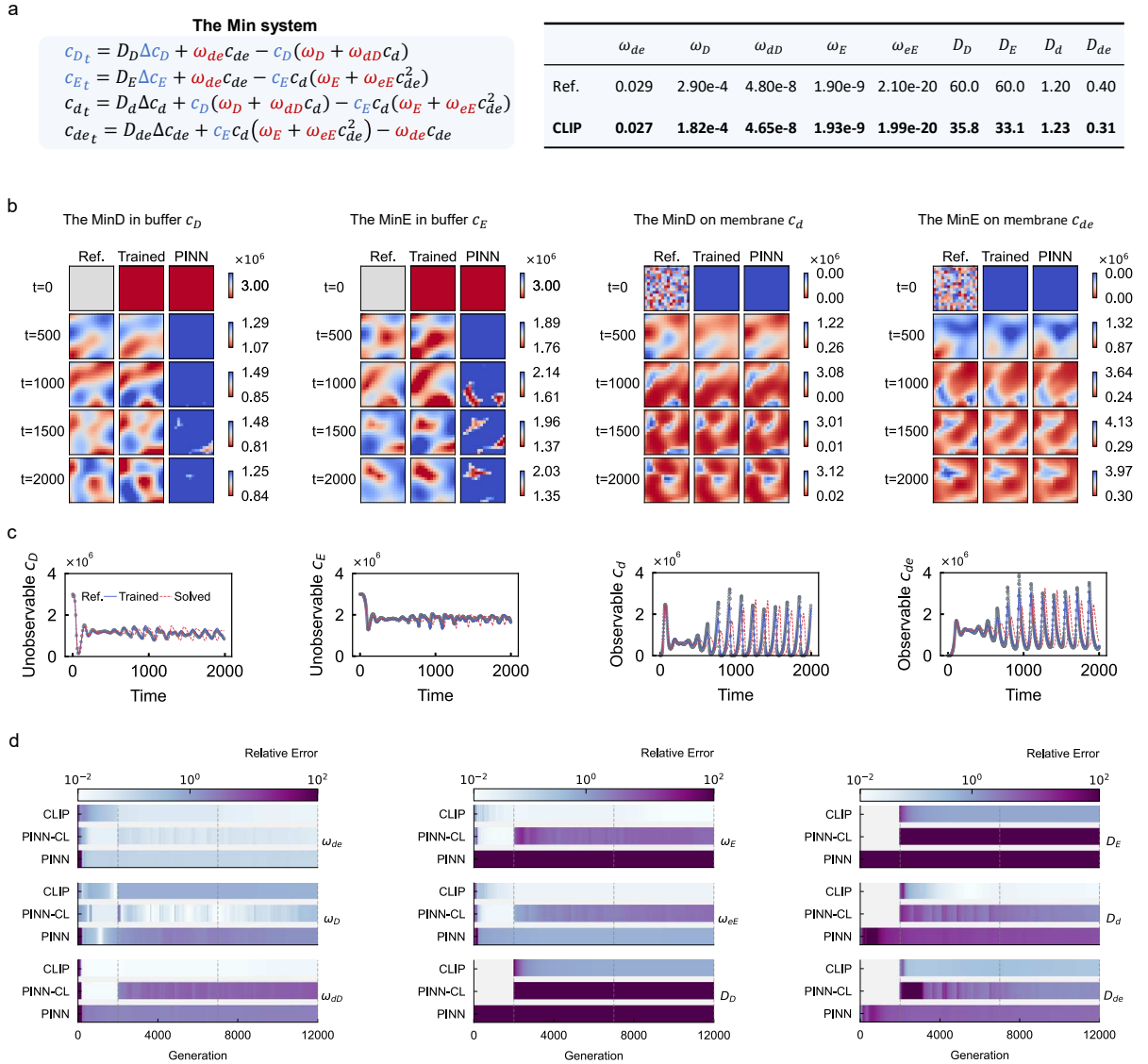


Fig. 3 Performance of CLIP framework on the Min proteins dynamics. **a.** The governing equations of the Min system, where blue denotes unobservable state variables and red indicates parameters to be identified. The table reports the reference values and the identified parameters on clean data. **b.** Reconstructed unobservable fields with comparisons to the baseline PINN. **c.** Single-point time series at the domain center. **d.** Relative errors of identified parameters from ablation on curriculum learning and anchored widening transfer learning.

becomes trapped in a suboptimal region. The non-convex structure of the loss landscape indicates the optimization difficulty of the baseline model. In contrast, Fig. 4b,c,d show that CLIP yields a smoother loss surface and more direct descent paths that follow local descent directions and appear approximately orthogonal to the projected loss contours. These results suggest improved

trainability and more reliable convergence under limited observations.

3 Discussion

In this work, we introduce CLIP, a physics-guided curriculum learning framework designed to resolve the ill-posed inverse problem of identifying parameters and reconstructing hidden states in partially

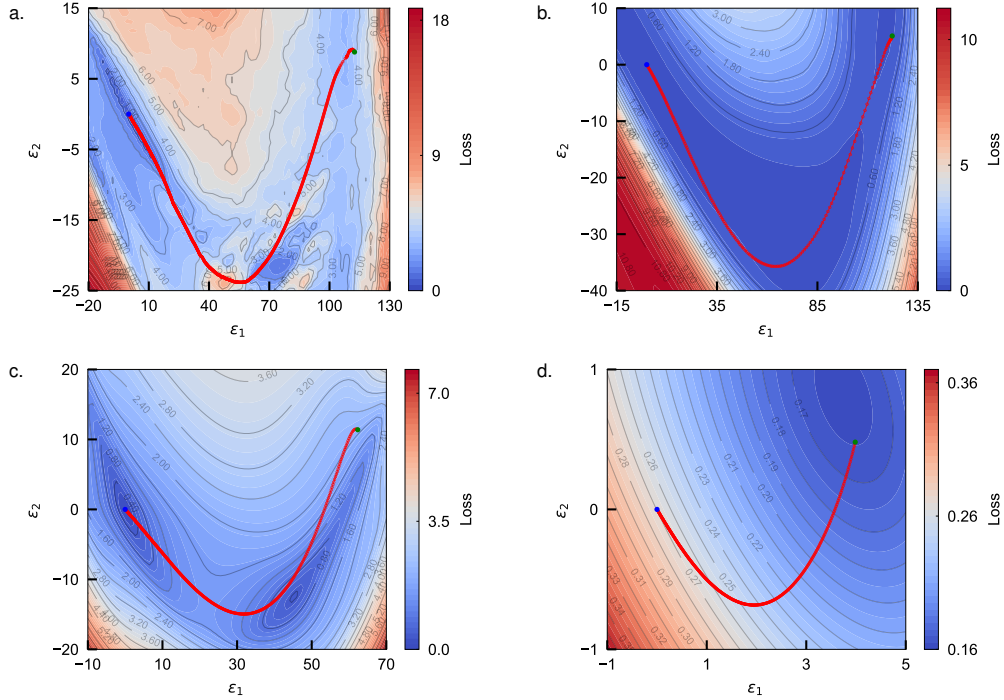


Fig. 4 Visualization of the loss landscape. Two-dimensional visualization of the loss surface and projected learning trajectories obtained by PCA. Green, blue, and red markers denote the training start, the converged solutions, and optimization trajectory, respectively. **a**, The loss surface of the baseline PINN results. **b-d**, The loss surface of the three successive stages of CLIP training.

observed reaction–diffusion systems. By synergizing a robust curriculum architecture with physical priors specific to RD dynamics, CLIP overcomes the optimization barriers that plague standard PINNs and gradient-free baselines.

The effectiveness of CLIP stems from the intrinsic spatiotemporal separability of reaction–diffusion patterns. Unlike convective flows like turbulence where spatial and temporal scales are inextricably mixed, RD systems often admit distinct regimes where local reaction kinetics dominate. By decomposing the learning process, CLIP effectively disentangles the identification of non-linear reaction topology (via the local ODE limit) from the estimation of transport coefficients (via the global PDE). This “divide-and-conquer” strategy aligns the optimization trajectory with the physical hierarchy of the system, preventing the vanishing gradient or local minima issues common when optimizing stiff, multi-scale objectives simultaneously. This principle suggests that similar curriculum designs could be adapted for

other multi-physics problems where distinct physical processes dominate different spatiotemporal regimes.

A critical innovation in our framework is the anchored widening transfer strategy. We observe that naively transitioning from the reaction-dominated curriculum to the full PDE regime often destabilizes the learned parameters. By anchoring the reaction features and expanding the network capacity to accommodate diffusive coupling, CLIP ensures a smooth traversal of the loss landscape. The visualization of the loss landscape in Fig. 4 confirms that this strategy improves the optimization path, avoiding the rugged non-convex basins that trap standard PINNs.

While CLIP demonstrates robust performance, several challenges remain. First, the current framework relies on the availability of initial conditions for the unobserved states. In experimental settings where latent fields are entirely unmeasured, the inverse problem may become non-unique. Future iterations could incorporate

delay-embedding techniques or probabilistic formulations to infer these initial states. Second, CLIP assumes the structure of the governing equations is known. Extending this framework to structure-free discovery, e.g., using symbolic regression or operator learning, represents a vital next step.

Finally, the potential of CLIP extends beyond standard RD systems. An exciting avenue for future research is the application to active matter, where reaction–diffusion processes couple with hydrodynamics. In such systems, the interplay between chemical signaling and fluid flow creates complex feedback loops. The progressive identification strategy proposed here, *i.e.* isolating chemical kinetics before coupling with advective transport, could prove essential for decoding the governing laws of biological self-organization and active fluids.

4 Methods

4.1 The CLIP Framework

Reaction-dominated Initialization

Curriculum learning [23] mimics human learning by presenting simpler tasks first and progressively increasing training difficulty. We adopt this principle to design the curriculum for training the model from easier subproblems to the full inverse problem. Specifically, we first focus on spatiotemporal regions where diffusion contributes weakly, thereby providing a stable initialization for subsequent joint identification of reaction and diffusion parameters. To identify such regions, the Laplacian operator with unit coefficient is applied to each observed state variable. We set the observed variables as $\{u_i\}_{i=1}^{N_m}$, where $N_m < N$ and N is the total number of state variables. However, when observations are noisy, directly computing Δu_i from measurements can be numerically unstable and leads to unreliable partitioning. We therefore employ a shallow multilayer perceptron (MLP) as a surrogate smoother to obtain a surrogate field $\tilde{\mathbf{u}}$, and then compute $\Delta \tilde{u}_i$ for mask generation. The surrogate $\tilde{\mathbf{u}}$ is used only to generate the mask, whereas all physics-informed training is performed on the original noisy observations to prevent bias from the smoothing step. We quantify diffusion

activity using

$$q_i(\mathbf{x}, t) = \Delta \tilde{u}_i(\mathbf{x}, t). \quad (2)$$

Intuitively, relatively small $|q_i|$ indicates weak spatial variation and thus a limited diffusion contribution, making these samples suitable for primary training. We then define the reaction-dominated mask as the intersection across observed variables,

$$M(\mathbf{x}, t) = \bigcap_{i=1}^{N_m} \mathbf{1} \left(\frac{|q_i(\mathbf{x}, t)|}{\max_{\mathbf{x}, t} (|q_i(\mathbf{x}, t)|)} < \tau \right), \quad (3)$$

where $\mathbf{1}(\cdot)$ is the indicator function and τ is a threshold. In all experiments, we use a fixed threshold, setting $\tau = 0.001$ for clean data and $\tau = 0.005$ for noisy data. The selected samples are then used to train the primary stage with a learning rate of 10^{-3} .

Diffusive coupling via transfer learning

In this stage, parameter identification transitions from the ODE setting to the full PDE, and the training dataset is obtained by uniform sampling over the full spatiotemporal domain to incorporate diffusion. Since diffusion operators introduce global spatial coupling across the spatiotemporal domain, naively fine-tuning the pretrained model often overwrites the reaction-related representations and coefficients learned in the primary stage and degrade coefficient estimation.

To stabilize this stage transition, we adopt an anchored widening transfer strategy that combines progressive widening with anchored inheritance. This design is inspired by the general ideas of progressive network expansion and parameter anchoring [29, 30]. Starting from the pretrained network, we widen each hidden layer by adding a small number of neurons per layer. The pretrained sub-network is then anchored by fine-tuning the inherited network parameters (including both weights and biases) across all layers, including the input layer and the shared trunk associated with the inherited units. In addition to the network parameters, the reaction-term coefficients are also treated as inherited variables. The inherited parameters are updated using a substantially reduced learning rate, ranging from 10^{-8} to 10^{-5} , while all other parameters are trained with

the default learning rate of 10^{-3} . In this way, the added degrees of freedom mainly capture diffusion effects, while the inherited reaction kinetics remain close to the primary stage solution.

Global fine-tuning with adaptive sampling

In the fine-tuning stage, we update all model parameters using a unified learning rate of 10^{-4} . To improve coverage of dynamically active regions, the training dataset is augmented using residual-based adaptive distribution (RAD) sampling. Specifically, given candidate spatiotemporal points $\{(\mathbf{x}_k, t_k)\}_{k=1}^{N^k}$, we denote by $\hat{\mathbf{u}}_\theta(\mathbf{x}, t) = (\hat{u}_\theta^1(\mathbf{x}, t), \dots, \hat{u}_\theta^N(\mathbf{x}, t))$ the network prediction of the N state variables, where θ collects the neural network parameters. For each candidate point k and each state variable indexed by i , we compute the PDE residual magnitude

$$\mathcal{R}_i(\mathbf{x}_k, t_k) = \partial_t \hat{u}_\theta^i - D_i \Delta \hat{u}_\theta^i - \mathcal{F}^i(\hat{\mathbf{u}}_\theta; \boldsymbol{\kappa}), \quad (4)$$

$$\varepsilon_k^i = |\mathcal{R}_i(\mathbf{x}_k, t_k)|. \quad (5)$$

The residuals of each variable are then normalized by their maximum value over the candidate set,

$$\tilde{\varepsilon}_k^i = \frac{\varepsilon_k^i}{\max_{1 \leq j \leq N_k} \varepsilon_j^i}, \quad (6)$$

and a pointwise score is formed by averaging over variables,

$$\bar{\varepsilon}_k = \frac{1}{N} \sum_{i=1}^N \tilde{\varepsilon}_k^i. \quad (7)$$

The discrete sampling distribution is then defined as

$$p_k = \frac{\bar{\varepsilon}_k}{\sum_{j=1}^{N_k} \bar{\varepsilon}_j}. \quad (8)$$

Additional training points are then sampled according to $\{p_k\}_{k=1}^{N_k}$. In this stage, the uniformly sampled dataset is augmented with an additional 10% RAD samples, relative to the original size.

4.2 Datasets

The numerical simulation data are generated using a spectral method with periodic boundary conditions. Table 2 summarizes the full spatial and temporal discretizations used in the simulations, and the training data are obtained by downsampling 2% of the grid points. To assess the robustness of the proposed CLIP approach,

gaussian noise is incorporated into the clean data as:

$$\mathbf{u}_{\text{obs}}(\mathbf{x}, t) = \mathbf{u}(\mathbf{x}, t) + \sigma \cdot \text{std}(\mathbf{u}(\mathbf{x}, t)) \cdot \mathcal{N}(0, 1), \quad (9)$$

where $\mathbf{u}(\mathbf{x}, t)$ denotes the noise-free solution and $\mathbf{u}_{\text{obs}}(\mathbf{x}, t)$ denotes the noisy observations. σ specifies the prescribed noise level, $\text{std}(u)$ is the standard deviation of u , and $\mathcal{N}(0, 1)$ stands for a standard normal random variable.

Table 2 Spatial–temporal discretization of datasets.

PDE	Domain (x, y, t)	Grid (N_x, N_y, N_t)
λ – ω RD	$[0, 20]^2 \times [0, 100]$	(64, 64, 1000)
Gray–Scott	$[0, 350]^2 \times [0, 100]$	(100, 100, 600)
Lotka–Volterra	$[0, 64]^2 \times [0, 100]$	(64, 64, 1000)
Min	$[0, 480]^2 \times [0, 2000]$	(64, 64, 2000)

4.3 Network architecture and optimization

We model the state field with a fully connected multi-task PINN [31]. The network takes spatiotemporal coordinates (\mathbf{x}, t) as input and outputs all states $\hat{\mathbf{u}}_\theta(\mathbf{x}, t)$. The architecture consists of a three-hidden-layer trunk shared across all variables and a one-hidden-layer branch for each state variable, enabling the sharing of common representations while retaining variable-specific features. From the middle stage onward, the width of each hidden layer is increased from 64 to 72 neurons for the three canonical cases, and from 128 to 144 neurons for the Min case. The activation functions are chosen according to signal characteristics. In particular, $\sin(\cdot)$ is used for the λ – ω system, the Lotka–Volterra system, and the Min system. For the Gray–Scott system with a stronger pulse-like periodic behavior, $\phi(x) = \text{ReLU}(\alpha \sin(x))$ with $\alpha = 0.1$ is used. All networks are initialized using Xavier initialization [32], and all trainable coefficients are initialized randomly in the interval $[0, 1]$. All experiments are implemented in PyTorch and executed on an NVIDIA GeForce RTX 3090 GPU.

To infer the reaction parameters $\boldsymbol{\kappa}$, diffusion coefficient D , and network parameters θ from partial observations, a PINN loss function is given

by

$$(\theta^*, \kappa^*, \mathbf{D}^*) = \arg \min_{\theta, \kappa, \mathbf{D}} \left(\mathcal{L}_{\text{data}} + \eta_{\text{pde}} \mathcal{L}_{\text{pde}} + \mathcal{L}_{\text{ic}} \right). \quad (10)$$

The L_1 loss is adopted for robustness to measurement noise, with only the first N_m state variables being observed. The losses are evaluated at the spatiotemporal collocation points $\{(\mathbf{x}_k, t_k)\}_{k=1}^{N_k}$ unless otherwise specified. The data loss is

$$\mathcal{L}_{\text{data}} = \frac{1}{N_m N_k} \sum_{i=1}^{N_m} \sum_{k=1}^{N_k} \left| \hat{u}_\theta^i - u_{\text{obs}}^i \right| \quad (11)$$

The physics loss penalizes violations of the reaction-diffusion equations across all state variables, including unobserved ones

$$\mathcal{L}_{\text{pde}} = \frac{1}{N N_k} \sum_{i=1}^N \sum_{k=1}^{N_k} \left| \partial_t \hat{u}_\theta^i - D_i \Delta \hat{u}_\theta^i - \mathcal{F}^i(\hat{\mathbf{u}}_\theta; \kappa) \right|. \quad (12)$$

At the initial time t_0 , initial conditions for all variables are evaluated at N_{k0} spatial points,

$$\mathcal{L}_{\text{ic}} = \frac{1}{N N_{k0}} \sum_{i=1}^N \sum_{k=1}^{N_{k0}} \left| \hat{u}_\theta^i(\mathbf{x}_k, t_0) - u_{\text{obs}}^i(\mathbf{x}_k, t_0) \right|. \quad (13)$$

The total loss is optimized using Adam optimizer [33]. Furthermore, the physics constraint is progressively strengthened during training by increasing η_{pde} . In the canonical cases, the PDE residual weight is initialized at $\eta_{\text{pde}} = 1$ in the primary stage and progressively increased up to 10, and is then re-initialized at 10 in the subsequent stages and further increased up to 30 during training. In the Min case, observations are normalized during training for numerical stability, whereas \mathcal{L}_{pde} is evaluated on the original scale. Accordingly, smaller values are adopted, with η_{pde} initialized at 10^{-7} in the primary stage, 10^{-5} in the middle stage, and 10^{-4} in the fine-tuning stage, and progressively increased during training according to the training stage. Since the Min coefficients span multiple orders of magnitude, kinetic parameters are optimized in log space. In addition, concentration products are rescaled using a characteristic concentration $c_0 = 10^5$ when evaluating the residual to reduce scale imbalance in the Min physics loss. Detailed network architectures, training hyperparameters, and

the update strategy for η_{pde} are provided in the Supplementary Information. All experiments were repeated with five different random seeds, with consistent results reported in the Supplementary Information.

4.4 Baseline methods

To benchmark parameter identification under partial observations, we compare CLIP against the ensemble Kalman filter (EnKF) and the representative gradient-free metaheuristic particle swarm optimization (PSO). The EnKF is an ensemble-based, derivative-free Bayesian method that updates system states and parameters by combining model forecasts with observations. We perform iterative parameter inference using the open-source DAFI framework [26], which enables PDE-constrained inverse problems. PSO is a population-based global optimization algorithm that simulates collective motion in swarms [27]. In this setting, PSO searches for physical parameters that minimize the mismatch between simulated and observed dynamics, providing a fully non-differentiable baseline for comparison. Additional implementation details for both baselines are provided in the Supplementary Information.

4.5 Evaluation metrics

To evaluate the performance of the CLIP framework, the relative absolute error (RAE) is used to quantify discrepancies between the reference coefficients and those identified by different methods (Fig. 2c, Fig. 2f, and Fig. 3i). The RAE provides an intuitive measure of identification accuracy and enables fair comparison across parameters with different physical scales.

For each coefficient ν_p , $p = 1, \dots, P$, the epoch-wise relative absolute error is defined as

$$\text{RAE}_{p,i} = \frac{|\nu_{p,i} - \nu_p^*|}{|\nu_p^*|}, \quad (14)$$

where ν_p^* denotes the reference value and $\nu_{p,i}$ is the estimated coefficient at training epoch i . This metric directly reflects the convergence behavior of each parameter during optimization.

To provide an overall quantitative comparison across parameters and methods, as reported in Table 1, we further compute the mean relative

absolute error (MRAE),

$$\text{MRAE} = \frac{1}{P} \sum_{p=1}^P \frac{|\nu_p^{\text{pred}} - \nu_p^*|}{|\nu_p^*|}, \quad (15)$$

where ν_p^{pred} denotes the final identified value of the p -th parameter.

4.6 Visualization of the loss landscape

To analyze the optimization behavior of CLIP, we visualize the loss landscape of the baseline PINN and CLIP together with their optimization trajectories. The high-dimensional loss is projected onto a two-dimensional subspace spanned by the principal directions of the optimization trajectory, following [28]. This visualization provides qualitative insight into the smoothness and curvature of the loss surface encountered during training. Implementation details are provided in the Supplementary Information.

Code availability. All the code and data necessary for reproducing the results is publicly available at <https://github.com/TurbSimGroupPKU/CLIP.git>.

Acknowledgments. This work has been supported by the National Natural Science Foundation of China (Grant Nos. 12588301, 12572247, and 12432010). Y.Z. also acknowledges the partial support from the Laoshan Laboratory Project under grant No. LSKJ202202000.

Authors' contributions. Y.Z., Y.C., and H.Z. designed the research. H.Z. implemented the algorithm and conducted the numerical experiments. Y.Z. managed the project. H.Z. wrote the initial manuscript. All authors discussed the results, revised the manuscript, and approved the final version.

Competing interests. The authors declare no competing interests.

References

[1] Daniele, S., Mantzaras, J., Jansohn, P., Denisov, A., Boulouchos, K.: Flame front/-turbulence interaction for syngas fuels in the thin reaction zones regime: turbulent and stretched laminar flame speeds at elevated pressures and temperatures. *Journal of Fluid Mechanics* **724**, 36–68 (2013)

[2] Loose, M., Fischer-Friedrich, E., Ries, J., Kruse, K., Schwille, P.: Spatial regulators for bacterial cell division self-organize into surface waves in vitro. *Science* **320**(5877), 789–792 (2008)

[3] Rathinam, M., Yu, M.: State and parameter estimation from exact partial state observation in stochastic reaction networks. *The Journal of Chemical Physics* **154**(3), 034103 (2021)

[4] Churchill, V., Chen, Y., Xu, Z., Xiu, D.: Dnn modeling of partial differential equations with incomplete data. *Journal of Computational Physics* **493**, 112502 (2023)

[5] Li, Z., Han, W., Zhang, Y., Fu, Q., Li, J., Qin, L., Dong, R., Sun, H., Deng, Y., Yang, L.: Learning spatiotemporal dynamics with a pretrained generative model. *Nature Machine Intelligence* **6**(12), 1566–1579 (2024)

[6] Stepaniants, G., Hastewell, A.D., Skinner, D.J., Totz, J.F., Dunkel, J.: Discovering dynamics and parameters of nonlinear oscillatory and chaotic systems from partial observations. *Physical Review Research* **6**(4), 043062 (2024)

[7] Ribera, H., Shirman, S., Nguyen, A., Mangan, N.: Model selection of chaotic systems from data with hidden variables using sparse data assimilation. *Chaos: An Interdisciplinary Journal of Nonlinear Science* **32**(6) (2022)

[8] Takens, F.: Detecting strange attractors in turbulence. In: *Dynamical Systems and Turbulence, Warwick 1980: Proceedings of a Symposium Held at the University of Warwick 1979/80*, pp. 366–381 (2006). Springer

[9] Wu, T., Gao, X., An, F., Sun, X., An, H., Su, Z., Gupta, S., Gao, J., Kurths, J.: Predicting multiple observations in complex systems through low-dimensional embeddings. *Nature Communications* **15**(1), 2242 (2024)

[10] Bakarji, J., Champion, K., Nathan Kutz, J., Brunton, S.L.: Discovering governing equations from partial measurements with deep delay autoencoders. *Proceedings of the Royal Society A: Mathematical, Physical and Engineering Sciences* **479**(2276), 20230422 (2023)

[11] Raissi, M., Yazdani, A., Karniadakis, G.E.: Hidden fluid mechanics: Learning velocity and pressure fields from flow visualizations. *Science* **367**(6481), 1026–1030 (2020)

[12] Lu, P.Y., Ariño Bernad, J., Soljačić, M.: Discovering sparse interpretable dynamics from partial observations. *Communications Physics* **5**(1), 206 (2022)

[13] Wang, S., Teng, Y., Perdikaris, P.: Understanding and mitigating gradient flow pathologies in physics-informed neural networks. *SIAM J. Sci. Comput.* **43**(5), 3055–3081 (2021)

[14] Wang, S., Yu, X., Perdikaris, P.: When and why pinns fail to train: A neural tangent kernel perspective. *Journal of Computational Physics* **449**, 110768 (2022)

[15] Krishnapriyan, A., Gholami, A., Zhe, S., Kirby, R., Mahoney, M.W.: Characterizing possible failure modes in physics-informed neural networks. In: *Advances in Neural Information Processing Systems*, vol. 34, pp. 26548–26560 (2021)

[16] Turing, A.M.: The chemical basis of morphogenesis. *Bulletin of Mathematical Biology* **52**(1), 153–197 (1990)

[17] Howard, J., Grill, S.W., Bois, J.S.: Turing’s next steps: the mechanochemical basis of morphogenesis. *Nature Reviews Molecular Cell Biology* **12**(6), 392–398 (2011)

[18] Kondo, S., Miura, T.: Reaction-diffusion model as a framework for understanding biological pattern formation. *science* **329**(5999), 1616–1620 (2010)

[19] Collinet, C., Lecuit, T.: Programmed and self-organized flow of information during morphogenesis. *Nature Reviews Molecular Cell Biology* **22**(4), 245–265 (2021)

[20] Banks, J., Veit, R.: Partial differential equations in ecology: spatial interactions and population dynamics. *Ecology* **75**(1), 17–29 (1994)

[21] Tan, Z., Chen, S., Peng, X., Zhang, L., Gao, C.: Polyamide membranes with nanoscale turing structures for water purification. *Science* **360**(6388), 518–521 (2018)

[22] Gu, J., Li, L., Xie, Y., Chen, B., Tian, F., Wang, Y., Zhong, J., Shen, J., Lu, J.: Turing structuring with multiple nanotwins to engineer efficient and stable catalysts for hydrogen evolution reaction. *Nature Communications* **14**(1), 5389 (2023)

[23] Bengio, Y., Louradour, J., Collobert, R., Weston, J.: Curriculum learning. In: *Proceedings of the 26th Annual International Conference on Machine Learning. ICML ’09*, pp. 41–48. Association for Computing Machinery, New York, NY, USA (2009)

[24] Wang, X., Chen, Y., Zhu, W.: A survey on curriculum learning. *IEEE transactions on pattern analysis and machine intelligence* **44**(9), 4555–4576 (2021)

[25] Wu, C., Zhu, M., Tan, Q., Kartha, Y., Lu, L.: A comprehensive study of non-adaptive and residual-based adaptive sampling for physics-informed neural networks. *Computer Methods in Applied Mechanics and Engineering* **403**, 115671 (2023)

[26] Ströfer, C.A.M.: Dafi: An open-source framework for ensemble-based data assimilation and field inversion. *Communications in Computational Physics* **29**(5), 1583–1622 (2021)

[27] Wang, D., Tan, D., Liu, L.: Particle swarm optimization algorithm: an overview. *Soft computing* **22**(2), 387–408 (2018)

[28] Li, H., Xu, Z., Taylor, G., Studer, C., Goldstein, T.: Visualizing the loss landscape of neural nets. *Advances in neural information processing systems* **31** (2018)

- [29] Rusu, A.A., Rabinowitz, N.C., Desjardins, G., Soyer, H., Kirkpatrick, J., Kavukcuoglu, K., Pascanu, R., Hadsell, R.: Progressive neural networks. arXiv preprint arXiv:1606.04671 (2016)
- [30] Xuhong, L., Grandvalet, Y., Davoine, F.: Explicit inductive bias for transfer learning with convolutional networks. In: International Conference on Machine Learning, pp. 2825–2834 (2018). PMLR
- [31] Ruder, S.: An overview of multi-task learning in deep neural networks. arXiv preprint arXiv:1706.05098 (2017)
- [32] Glorot, X., Bengio, Y.: Understanding the difficulty of training deep feedforward neural networks. In: Proceedings of the Thirteenth International Conference on Artificial Intelligence and Statistics, pp. 249–256 (2010)
- [33] Kinga, D., Adam, J.B., *et al.*: A method for stochastic optimization. In: International Conference on Learning Representations (ICLR), vol. 5 (2015)

Supplementary Information for: Physics-guided curriculum learning for the identification of reaction–diffusion dynamics from partial observations

Hanyu Zhou¹, Yuansheng Cao² and Yaomin Zhao^{1*}

¹*HEDPS, Center for Applied Physics and Technology, and School of Mechanics and Engineering Science, Peking University, Beijing, 100871, China.

²Department of Physics, Tsinghua University, Beijing, 100084, China.

*Corresponding author(s). E-mail(s): yaomin.zhao@pku.edu.cn;
Contributing authors: hanyuzhou@stu.pku.edu.cn; yscao@tsinghua.edu.cn;

1 Detailed baseline implementations

As a representative gradient-free baseline, we consider an ensemble Kalman filter (EnKF) based approach for PDE parameter identification under partial observations. We use the open-source DAFI framework [1], which implements ensemble-based, derivative-free Bayesian methods for PDE-constrained inverse problems. The unknown physical parameters are treated as an augmented state and are inferred using an iterative EnKF procedure. In each iteration, ensemble members are propagated by the same forward PDE solver used in our main experiments, and the simulated outputs are mapped to the observation space for data assimilation. An ensemble size of 50 members is used throughout all experiments. The initial ensemble is drawn from a Gaussian prior with unit-scale mean 1.0 and moderate variance 0.1. At each iteration, we assimilate all available observations without spatial or temporal subsampling. This EnKF approach provides a fully non-differentiable, simulation-driven Bayesian baseline for comparison.

As another representative gradient-free baseline, particle swarm optimization (PSO) [2] is employed for PDE parameter identification under partial observations. We adopt a standard global-best PSO with inertia weight formulation, where each particle represents a candidate set of physical parameters. Particle velocities are updated using fixed acceleration coefficients $C_1 = C_2 = 1.5$ and a constant inertia weight, following the canonical PSO update rule. A maximum velocity constraint is imposed to prevent unstable updates. The swarm size is set to 100 particles. Parameters of particles are initialized by random sampling within bounded ranges determined from an initial parameter guess, where the initial guess is sampled from the interval $(0, 1]$. Due to the strong nonlinearity of the PDE solver and partial observability, many randomly sampled parameter combinations lead to invalid simulations. To ensure a valid initial swarm, particles are repeatedly initialized by random sampling within predefined parameter bounds until 100 feasible parameter sets yielding successful PDE simulations are obtained. The fitness function is defined as the mismatch between simulated and observed dynamics, evaluated only on observable variables and locations. Each fitness evaluation requires a full forward PDE simulation. Considering the high computational cost associated with both initialization and forward solves, the solution obtained at

2 *Supplementary Information*

1,000 iterations is reported as the final result for comparison. PSO thus provides a fully non-differentiable, simulation-driven baseline for evaluating parameter identification performance. It should be noted that all EnKF and PSO hyperparameters are chosen following standard practice and are not tuned to individual test cases.

2 Detailed ablation experiments

This section presents ablation experiments designed to assess the contributions of curriculum learning and anchored widening transfer to parameter identification and hidden-state reconstruction in partially observable reaction–diffusion systems. We compare three training strategies: a baseline PINN, a baseline PINN with curriculum learning, and a baseline PINN with both curriculum learning and anchored widening transfer, referred to as CLIP. All three strategies use the same data loss formulation and initial-condition constraints for unobserved variables. For the Min example, the parameters are also optimized in log-space, and the PDE residual is evaluated using the same scaling as in the main text, including the characteristic concentration c_0 .

Baseline PINNs are trained directly on the full spatiotemporal domain without curriculum masking or anchored widening transfer. Training points are obtained by uniform sampling at a rate of 2% of the full grid. The total number of optimization steps matches that of CLIP. To avoid capacity disadvantages, the network architecture is chosen to match the CLIP architecture used in the middle stage, which is the first full-domain PDE training stage. The optimizer is Adam with a learning rate of 10^{-3} . Throughout training, the PDE residual is evaluated using the full RD equations, including all reaction and diffusion terms as well as their associated coefficients. The PDE residual weight η_{pde} follows the same growth strategy as in CLIP, increasing linearly from 10 to 30 in the canonical cases. For the Min system, η_{pde} is increased from 10^{-7} to 10^{-4} according to a linear schedule, using the same iteration update criterion as in the CLIP middle stage.

In the second experiment, curriculum learning is introduced without network widening or anchoring. Training consists of a primary stage followed by full-domain training. The network architecture is fixed throughout and matches that used in the CLIP middle stage. The optimizer remains Adam with a learning rate of 10^{-3} in both stages. During the primary stage, training points are sampled exclusively from reaction-dominated regions using the same mask construction and sampling strategy as in CLIP. The PDE residual is evaluated using only reaction terms and their associated coefficients, and the number of optimization steps in the primary stage matches that of CLIP. Subsequently, training continues on the full spatiotemporal domain with uniform sampling until the total number of iterations aligns with CLIP. The PDE residual weight η_{pde} follows the same update rule as in CLIP when transitioning from the primary to the middle stage.

The third experiment, CLIP, is described in the main text, and all remaining training details follow the main-text specification.

3 Repeatability across random initializations

We evaluate robustness on the canonical systems by repeating experiments on clean data with different random initializations. For each system, five physically admissible solutions are collected, requiring positive diffusion coefficients and non-negative reconstructed state variables. Box plots of the resulting parameter errors are shown in Fig. 1.

The annotations in Fig. 1 report the mean and standard deviation of the relative parameter errors over five repeated runs with different random initializations. Among the canonical systems, the λ - ω RD system exhibits the smallest variance across runs, reflecting its relatively simple dynamics. The Lotka–Volterra system remains stable despite involving six unknown parameters, with moderate variability across repeated experiments. The Gray–Scott system shows slightly larger variance, which can be attributed to its pulse-like spatiotemporal patterns and spiral-wave dynamics. Nevertheless, its variability remains substantially smaller than that of the baseline PINN and other comparison methods. For all systems, the

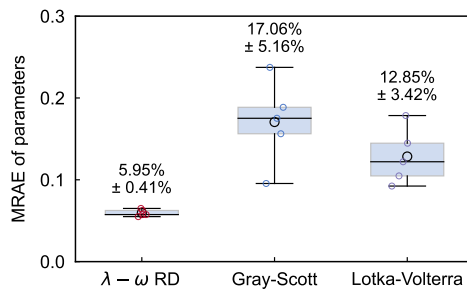


Fig. 1 Robustness of parameter identification using the CLIP framework on canonical systems

results reported in the main text correspond to the parameter set that yields the smallest observation error when the identified coefficients are used to re-simulate the governing equations.

4 Training hyperparameters

Hyperparameters are fixed prior to training and are not tuned separately for individual systems. Tables 1 and 2 summarize the specific architecture and optimization hyperparameters used in all experiments. Unless explicitly listed, shared settings such as the sampling rate, parameter initialization and optimizer type are fixed across systems and follow the descriptions in the main Methods.

Table 1 System-specific network architecture and activation functions.

System	Trunk width	Branch width	Widened width	Activation
$\lambda - \omega$	64	64	72	$\sin(x)$
Gray-Scott	64	64	72	$\text{ReLU}(\alpha \sin x)$, $\alpha = 0.1$
Lotka-Volterra	64	64	72	$\sin(x)$
Min	128	128	144	$\sin(x)$

Table 2 System-specific optimization and loss hyperparameters.

System	Epoch				Learning rate	
	Prim.	Mid.	Fine	Prim.	Mid.(anchored, normal)	Fine
$\lambda - \omega$	1000	2000	2000	10^{-3}	$10^{-5}, 10^{-3}$	10^{-4}
Gray-Scott	2000	5000	5000	10^{-3}	$10^{-8}, 10^{-3}$	10^{-4}
Lotka-Volterra	2000	5000	5000	10^{-3}	$10^{-8}, 10^{-3}$	10^{-4}
Min	2000	5000	5000	10^{-3}	$10^{-6}, 10^{-3}$	10^{-4}

The weight of the PDE residual term, η_{pde} , is progressively increased during training according to an adaptive update rule given in Algorithm 1. The corresponding update parameters for each system and training stage are summarized in Table 3. The threshold τ_{data} is not applied in the canonical RD cases, whereas for the Min system it is set to 0.05 to stabilize training. Together, these tables and the update rule specify the training configuration used throughout this work.

Algorithm 1 PDE residual weight η_{pde} update during training.

Require: Current epoch e , data loss $\mathcal{L}_{\text{data}}(e)$, last growth epoch e_{last}
Require: Threshold τ_{data} , growth interval Δe , increment $\Delta\eta$, maximum η_{max}

```

1:  $\eta \leftarrow \eta_{\text{pde}}(e)$ 
2: if  $\mathcal{L}_{\text{data}}(e) < \tau_{\text{data}}$  and  $(e - e_{\text{last}}) \geq \Delta e$  then
3:    $\eta \leftarrow \min(\eta + \Delta\eta, \eta_{\text{max}})$ 
4:    $e_{\text{last}} \leftarrow e$ 
5: end if
6: return  $\eta$ 

```

Table 3 Parameters of the adaptive PDE residual weighting strategy (Algorithm 1).

System	η_{init}			$\Delta\eta$			Δe			η_{max}		
	Prim.	Mid.	Fine	Prim.	Mid.	Fine	Prim.	Mid.	Fine	Prim.	Mid.	Fine
$\lambda-\omega$ RD	1	1	1	0	0	0	-	-	-	-	-	-
Gray–Scott	1	10	10	5×10^{-3}	5×10^{-3}	5×10^{-3}	1	1	1	30	30	30
Lotka–Volterra	1	10	10	5×10^{-3}	5×10^{-3}	5×10^{-3}	1	1	1	30	30	30
Min	10^{-7}	10^{-5}	10^{-4}	10^{-7}	10^{-6}	10^{-6}	200	50	50	10^{-3}	10^{-3}	10^{-3}

5 Visualization of the loss landscape

To compare the optimization behavior, we visualize the loss landscape of the baseline PINN and the CLIP together with their learning trajectories. Since the parameter space of neural networks is high-dimensional, the loss function is projected onto a two-dimensional subspace, where it can be evaluated on a grid for visualization. Following Li et al. [3], we select a reference point θ^* and two orthogonal directions δ and η , and define the projected loss surface as

$$f(\alpha, \beta) = \mathcal{L}(\theta^* + \alpha\delta + \beta\eta), \quad (1)$$

where \mathcal{L} denotes the complete PINN loss and (α, β) are scalar coordinates parameterizing the two-dimensional subspace. The directions δ and η are computed using principal component analysis (PCA) applied to the parameter trajectory during optimization. Specifically, we collect the model parameters $\{\theta_i\}_{i=0}^{n-1}$ along training and construct the matrix $M = [\theta_0 - \theta_n; \dots; \theta_{n-1} - \theta_n]$ from which the first two principal directions are extracted and denoted by δ and η . The optimizer trajectory is then projected onto this two-dimensional subspace by computing the corresponding (α, β) coordinates at each training iteration. The loss surface is visualized by evaluating $f(\alpha, \beta)$ over a grid chosen to cover the projected optimization trajectories. For more details on this procedure, see [3].

References

- [1] Ströfer, C.A.M.: Dafi: An open-source framework for ensemble-based data assimilation and field inversion. *Communications in Computational Physics* **29**(5), 1583–1622 (2021)
- [2] Wang, D., Tan, D., Liu, L.: Particle swarm optimization algorithm: an overview. *Soft computing* **22**(2), 387–408 (2018)
- [3] Li, H., Xu, Z., Taylor, G., Studer, C., Goldstein, T.: Visualizing the loss landscape of neural nets. *Advances in neural information processing systems* **31** (2018)